JGR Atmospheres

RESEARCH ARTICLE
10.1029/2023JD039958

Inconsistent 3-D Structures and Sources of Sulfate Ammonium and Nitrate Ammonium Aerosols During Cold Front Episodes

Wei Peng[1,2], Bin Zhu[1], Hanqing Kang[1], Kui Chen[1], Wen Lu[1], Chunsong Lu[1], Na Kang[1], Jianlin Hu[3], Haishan Chen[1], and Hong Liao[3]

[1]Key Laboratory of Meteorological Disaster, Ministry of Education (KLME), Joint International Research Laboratory of Climate and Environment Change (ILCEC), Collaborative Innovation Center on Forecast and Evaluation of Meteorological Disasters, Key Laboratory for Aerosol-Cloud-Precipitation of China Meteorological Administration, Nanjing University of Information Science & Technology, Nanjing, China, [2]Hunan Meteorological Information Center, Hunan Meteorological Bureau, Changsha, China, [3]Jiangsu Key Laboratory of Atmospheric Monitoring and Pollution Control, Collaborative Innovation Center of Atmospheric Environment and Equipment Technology, School of Environmental Science and Engineering, Nanjing University of Information Science & Technology, Nanjing, China

Key Points:

- Uplifted by cold fronts, the temperature-sensitive NH_4NO_3 forms in the upper BL and dissociates in the lower BL
- $(NH_4)_2SO_4$ forms in the whole BL because it is highly thermally stable and impervious to dissociation
- The differences in thermostability and lifetime result in local sources being dominant for NH_4NO_3, while upstream sources dominate for $(NH_4)_2SO_4$

Correspondence to:
B. Zhu,
binzhu@nuist.edu.cn

Citation:
Peng, W., Zhu, B., Kang, H., Chen, K., Lu, W., Lu, C., et al. (2024). Inconsistent 3-D structures and sources of sulfate ammonium and nitrate ammonium aerosols during cold front episodes. *Journal of Geophysical Research: Atmospheres*, *129*, e2023JD039958. https://doi.org/10.1029/2023JD039958

Received 8 SEP 2023
Accepted 18 MAR 2024

Abstract Since the distinct thermostability difference of sulfate ammonium and nitrate ammonium aerosols, their distributions, evolutions and sources could be unpredictable on a long-range transport condition. Here, we highlighted the 3-D structures and sources of SO_4^{2-}, NO_3^- and NH_4^+ (SNA) during two cold front episodes in east China. Cold fronts effectively uplift and transport $PM_{2.5}$ and its precursors from upstream sources to the Yangtze River Delta (YRD). Specifically, in the YRD, surface SO_4^{2-} is mostly imported from the upstreams, accounting for ~48%, significantly higher than the contribution from the YRD itself (~29%). In contrast, NH_4NO_3 is thermally unstable and more easily lost in the warmer and lower boundary layer (BL) ahead of cold front. Consequently, only 20% of the total NO_3^- originates from upstreams, while the YRD contributes 28%. In the upper BL, the contribution of SO_4^{2-} from upstreams remain high (~49%), with only 18% originating from the YRD. However, due to the intense thermostability of NH_4NO_3 in colder and wetter air, the YRD's contribution to NO_3^- is 27%, and upstreams contribute 20%. The physical processes exert relatively consistent effects on variations of $PM_{2.5}$ and SNA concentrations. The aerosol chemical process (AERO) of $(NH_4)_2SO_4$ consistently contributes positively throughout the entire BL. Conversely, the temperature-sensitive NH_4NO_3 undergoes repeated dissociation/condensation and deposition, causing positive AERO contributions in upper BL and negative contributions in lower BL. Results indicate that one difference in physicochemical property of species could induce their distinct distributions and sources in large scale, and should be considered in regional air pollution control.

Plain Language Summary Long-range transport of $PM_{2.5}$ by cold frontal passage is an important haze formation mechanism. Previous field and modeling studies have revealed that the vertical distribution of particle sulfate and particle nitrate concentrations varied significantly. However, few studies have explored the 3-D structures and sources of particle sulfate and nitrate under a long-range transport conditions. In this study, we used combined observations and model simulations during cold front events to address the unrevealed inconsistent 3-D structures and sources of sulfate and nitrate resulting from temperature stability differences. Cold front episodes redistribute SNA and precursors in three dimensions, driven by drastic meteorology changes and long range transport. Consequently, the distributions, variations and sources of SNA may exhibit complexity and unpredictablility during long-range transport. Specificlly, $(NH_4)_2SO_4$ is mostly imported from the upstream in the whole boundary layer (BL), but NH_4NO_3 is dominant by local source. Moreover, uplifting by cold front, temperature-sensitive NH_4NO_3 form in the upper BL and dissociation in the lower BL, whereas $(NH_4)_2SO_4$ forms uniformly across the whole BL. These findings suggest that one difference in physicochemical property of species can induce distinct distributions and sources in large scale, highlighting the importance of considering such differences in regional air pollution control.

1. Introduction

Since the implementation of the Atmospheric Pollution Prevention and Control Action Plan in 2013, particulate concentrations, particularly $PM_{2.5}$ and sulfate aerosol, have sharply declined in central-eastern China (Wei

et al., 2017). However, the changes of nitrate aerosol are not as significant, making it the main inorganic aerosol in eastern China (Ding et al., 2019; Xu et al., 2019). SO_4^{2-}, NO_3^- and NH_4^+, collectively referred to as SNA, are the main components of $PM_{2.5}$ (Fan et al., 2015). They are soluble in water, volatile, and can be partitioned between the gas and particulate phases. There are three mechanisms for SNA formation: gas-to-particle conversion, which is the primary mechanism through the neutralization of NH_3 with H_2SO_4 and HNO_3 (Hu et al., 2008); atmospheric oxidation of precursors such as SO_2, DMS, NO_x and HNO_2 to form acidic gases such as H_2SO_4 and HNO_3; and formation through heterogeneous chemical and transformation processes on the surface of particles (Zhao et al., 2013; Zhao et al., 2013). SNA has substantial regional and worldwide consequences on the climate, the ecosystem, and human health (Vang et al., 2013; Wang et al., 2014).

The factors driving the formation mechanism of $PM_{2.5}$ pollution in China remain unclear due to the intricate interactions among pollution sources, meteorology, and atmospheric chemical processes (Guo et al., 2014). Among these factors, precursor emissions, unfavorable meteorological conditions, the formation of secondary aerosols, and regional transport of particulate matter all contribute to particulate pollution (Pang et al., 2020). For example, Huang et al. (2020) and Kang et al. (2019) pointed out that southward-moving cold fronts accompanied by strong northerly winds remove haze pollution from the North China Plain (NCP) but transport pollution from the NCP to its downstream Yangtze River Delat (YRD). Sun et al. (2019) found that nitrate concentrations are influenced by regional transport from northern China. Observations revealed that about 63% of the haze events occurring in the YRD are attributed to long-range transport caused by cold fronts (Liu et al., 2021).

During $PM_{2.5}$ pollution events, $PM_{2.5}$ concentrations increase significantly, which accompanied by an increase in the proportions of secondarily formed SNA (Zheng et al., 2015). Typically, NH_4NO_3 formation occurs only when NH_3 is enriched after completely neutralizing H_2SO_4 with NH_3. In wintertime, nitrate mass concentrations are generally higher than sulfate concentrations and predominate the SNA composition (Sun et al., 2020; Xu et al., 2019). Chemical thermodynamic characteristics are linked to the formation of SNA and their compositions. For example, temperature can adjust aerosol concentrations by affecting the chemical reaction rate of precursors and changing the gas-particle equilibrium constant. The gas-particle equilibrium of NH_4NO_3 is more temperature-sensitive than that of $(NH_4)_2SO_4$. The lower temperature shifts the system equilibrium to the aerosol phase, thus increasing NH_4NO_3 concentrations (Pathak et al., 2009; Wang et al., 2020). As HNO_3 is deposited at a much higher rate than NO_3^-, when NH_3 is insufficient to significantly neutralize HNO_3, the formation of particle nitrate can be reduced (Zhai et al., 2021). Under NH_3-rich and high relative humidity conditions, NO_3^- is considered to be formed mainly by enhanced heterogeneous reactions (Ge et al., 2019; Shao et al., 2018). However, the relative humidity and precursor SO_2 are major factors influencing sulfate formation, and significant reductions of SO_2 emissions inhibit sulfate formation (Ding et al., 2019; Li et al., 2019).

Because of the distinct thermostability and lifetime difference between sulfate ammonium and nitrate ammonium aerosols, as well as differences in emissions of SNA and precursors between upstream and downstream regions (Saikawa et al., 2017), the distributions, variations and sources of SNA may be complex and unpredictable during long range transport (Figure 1). Cold front episodes can redistribute SNA and precursors in three dimensions with drastic changes in meteorological elements (Kang et al., 2021). Previous studies have revealed differences in concentration distribution of sulfate and nitrate vertically by in-situ observations and urban-scale model simulations (Sun et al., 2020). However, few studies have clearly revealed the inconsistent three-dimensional (3-D) structures, evolution and sources of these components under a long-range transport condition. To further understand the 3D structures and evolution of SNA under cold frontal intrusion periods, the 3-D distribution of SNA and regional sources were investigated during two cold front episodes in eastern China from 15 to 20 January 2019, using the Weather Research and Forecasting (WRF) mesoscale meteorological model and the Community Multiscale Air Quality (CMAQ) modeling system coupled with the integrated source apportionment method (ISAM). Combined with the field experiments on boundary layer (BL) air pollution and meteorology conducted in Nanjing, the results highlight the regional source apportionment, and the physical and chemical processes that control SNA distributions along cold frontal passage in eastern China.

2. Data, Methodology and Model

In this study, CMAQv5.3.2 was used to simulate chemical processes and transport diffusion processes of gaseous and particulate, and WRFv3.9.1 was employed to simulate the meteorological fields required to drive the CMAQ model. The Observation Nudging method implemented in WRF aided in improving the model prediction

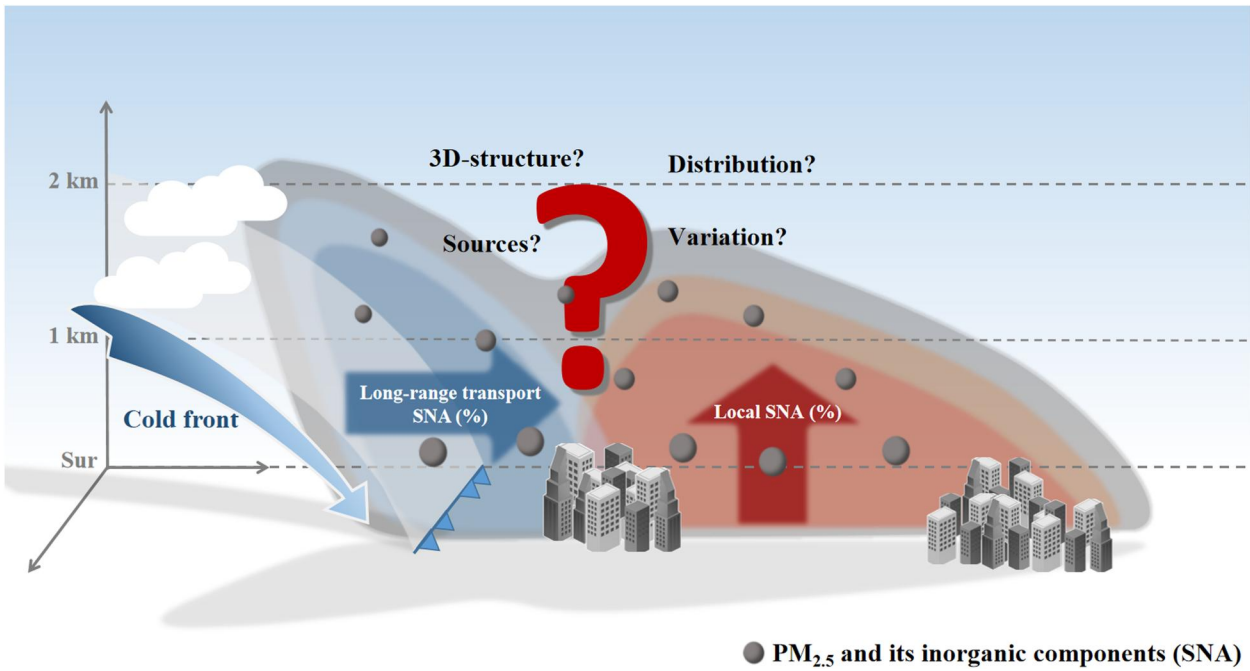

Figure 1. How does a cold front specifically affects the three-dimensional structure of $PM_{2.5}$ and its inorganic components, for example, sulfate, nitrate and ammonium? The gray dots indicate $PM_{2.5}$ particles, yet lack detailed information on distributions, variations and sources of SNA due to their thermodynamic features under the cold front passage (the blue arrow) with sharply changed meteorology. The blue and red shadow indicate the cold and polluted air masses transported over long distance, and the warm and humid local air masses, respectively.

accuracy (Liu et al., 2008). The simulation area and source regions as shown in Figure 2. The simulation domain covered East China, the Korean Peninsula, and the surrounding ocean with 10 × 10 km horizontal resolution and 220 × 220 grids, centered at 33.5°N and 118°E. We divided the WRF-CMAQ model vertically into 37 sigma levels from the surface to the top of the troposphere, with 7 levels below 1 km. The anthropogenic emissions we adopted were based on the Multi-resolution Emission Inventory for China (MEIC, 2016 version, http://www.meicmodel.org/) provided by Tsinghua University (Li et al., 2017), and biogenic emissions were generated by the Model of Emissions of Gases and Aerosols from Nature (MEGAN) version 2.1 (Guenther et al., 2012). The initial meteorological and boundary conditions of the simulated area we used to drive the WRF model were provided by the National Center for Environmental Prediction (NCEP) Final (FNL) meteorological field data at a 0.25° × 0.25° horizontal spatial resolution (National Centers for Environmental Prediction/National Weather Service/NOAA/U.S. Department of Commerce, 2015). We adopted the Mellor-Yamada-Janjic TKE scheme (Janjić, 1994; Petäjä et al., 2016) as the boundary layer scheme, and we utilized the gas-phase chemical mechanism CB06 coupled with the AERO7 aerosol scheme in the CMAQ model (Appel et al., 2021). We used the initial chemical and boundary conditions (ICON and BCON) drive the CMAQ model were provided by the outputs of the Community Atmosphere Model with Chemistry (CAM-Chem) based on MOZART2CAMX (Lamarque et al., 2012). The simulation ran from 00:00 UTC 10 January 2019 to 00:00 UTC 25 January 2019, with the first 5 days used as the spin-up time.

The process analysis technique, coupled with the CMAQ model, can determine the contribution of physical and chemical processes to the simulated species (Byun & Ching, 1999). We used the process analysis to calculate the physical and chemical processes include horizontal advection (HADV), vertical advection (VADV), vertical dispersion (VDIF), dry deposition (DDEP), cloud processes and aqueous chemistry (CLDS), aerosol (AERO) and emission (EMIS) processes, to analyze pollution causes specifically. The integrated source apportionment method (ISAM) within the CMAQ model that we used, tracked the contributions of ICONs, BCONs, and user-defined source regions to ambient and deposited gases and aerosol particles (Kwok et al., 2013). Currently, ISAM supports two $PM_{2.5}$ tags: a primary species tag tracks elemental carbon, organic carbon, sulfate, nitrate, ammonium, and other trace elements (e.g., Cl, Na, K, Fe, Ca, Al, Si, Ti, Mn); another tag tracks the secondary

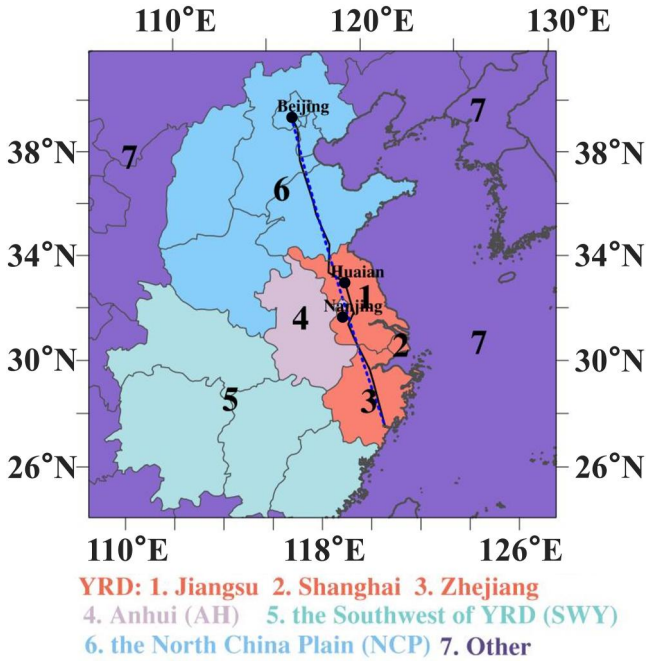

Figure 2. Modeling domain and source regions. Black dots denote the locations of observation sites in Beijing, Huaian, and Nanjing. The solid black line connects 14 observation sites from the north of the North China Plain (NCP) to the south of the Yangtze River Delta (YRD). The dashed blue line indicates the location of the vertical cross section shown in Figure 5. The emission from Yangtze River Delta (YRD) is considered as local source. Emissions from the North China Plain (NCP), Anhui (AH), the Southwest of YRD (SWY) and other regions are considered as long-range transport sources.

formation of sulfate, nitrate, ammonium and all gases associated with secondary aerosol species formations (e.g., SO_2, NO_2, NO, NO_3, HNO_3, HONO, N_2O_5, PAN, and NH_3).

We carried out a meteorological and atmospheric pollution field experiment in the boundary layer, as well as ground-based SNA online observations in the northern suburb of Nanjing City (32. 2°N, 118. 7°E) between 12 and 20 January 2019. An unmanned aerial vehicle (UAV) platform equipped with meteorological sensors and aerosol monitoring instrument (Thermo Mie PDR-1500) was employed to measure the vertical profiles of meteorological parameters and $PM_{2.5}$ concentrations in the boundary layer up to approximately 1,000 m, with a temporal resolution of 3 hr (Shi et al., 2021). Mornitor for AeRosols and Gases in ambient Air (MARGA) was deployed over the entire period to determine the chemical composition of water-soluble inorganic ions (SO_4^{2-}, NO_3^-, NH_4^+, Cl^-, Ca^{2+}, K^+, Na^+, Mg^{2+}), and trace gases (NH_3, SO_2, HONO, HNO_3, and HCl) with an hourly time-resolution (Griffith et al., 2015; Rodelas et al., 2019). The detection limits for water-soluble inorganic ions were 0.04, 0.06, 0.01, 0.05, 0.09, 0.05, 0.50, and 0.10 $\mu g \cdot m^{-3}$, respectively, for trace gases were 0.08, 0.05, 0.08, 0.05 and 0.10 $\mu g \cdot m^{-3}$, respectively. Ground-based $PM_{2.5}$ data from other areas were obtained from the China air quality online monitoring and analysis platform (https://www.aqistudy.cn/) provided by the Ministry of Ecology and Environment of China, and the ground-based observations of meteorological parameters were derived from America National Centers for Environmental Information (https://www.ncei.noaa.gov/).

Air mass backward trajectories were calculated by the Hybrid Single-Particle Lagrangian Integrated Trajectory (HYSPLIT) model, implemented in the MeteoInfo tool (Wang et al., 2009), developed by the National Oceanic and Atmospheric Administration (NOAA) (Rolph et al., 2017; Stein et al., 2015). The meteorology data utilized to drive the HYSPLIT model were derived from the National Centers for Environmental Prediction Global Data Assimilation System (GDAS), provided by the US National Center for Environmental Prediction (NCEP), with a horizontal resolution of 1°.

3. Results and Discussion

3.1. Model Validation

To evaluate the model's performance in reproducing pollutants and meteorological parameters, Figure 3 shows the vertical distributions of simulated and observed $PM_{2.5}$ concentrations and meteorological factors (RH, T, and wind vectors) in Nanjing during the pollution period. Result indicates an acceptable agreement between the model simulation and UAV observations for both $PM_{2.5}$ and meteorological factors. Simulated and observed results of near-surface SO_4^{2-}, NO_3^-, and NH_4^+ in Nanjing are further compared in Figure 4. The daily variation of SNA showed a bimodal distribution. The SNA gradually accumulated at night and maintained at higher concentration levels than in daytime. The SNA peaked in the morning around 10:00-12:00 LT and then began to decline and reached its lowest concentration in the afternoon around 15:00–17:00 LT. This pattern is mainly due to the increase in boundary layer height and enhanced vertical diffusion of pollutants. In winter, NO_3^- concentration varies more slightly than SO_4^{2-} throughout the day, consistent with observation by Sun et al. (2019), as discussed in Section 3.3. The concentration of NH_4^+ is affected by SO_4^{2-} and NO_3^- under NH_3-rich conditions. However, the simulation without the bidirectional treatment of ammonia fluxes may underpredicts NH_3 concentrations, especially in warm season and agriculture areas (Pleim et al., 2013, 2019). While in the cold front episodes, NH_4^+ from upstream and local sources may be overestimated and underestimated in a small extend, respectively, without considering bidirectional ammonia fluxes. The model predicted molar concentration ratios of SO_4^{2-}, NO_3^-, and NH_4^+ were 6.5%, 40.4%, and 53.1%, respectively, with SNA contributing 62.0% of $PM_{2.5}$ mass concentrations. The observed SNA molar concentration accounted for 8.0%, 40.0%, and 13.0%, respectively, with

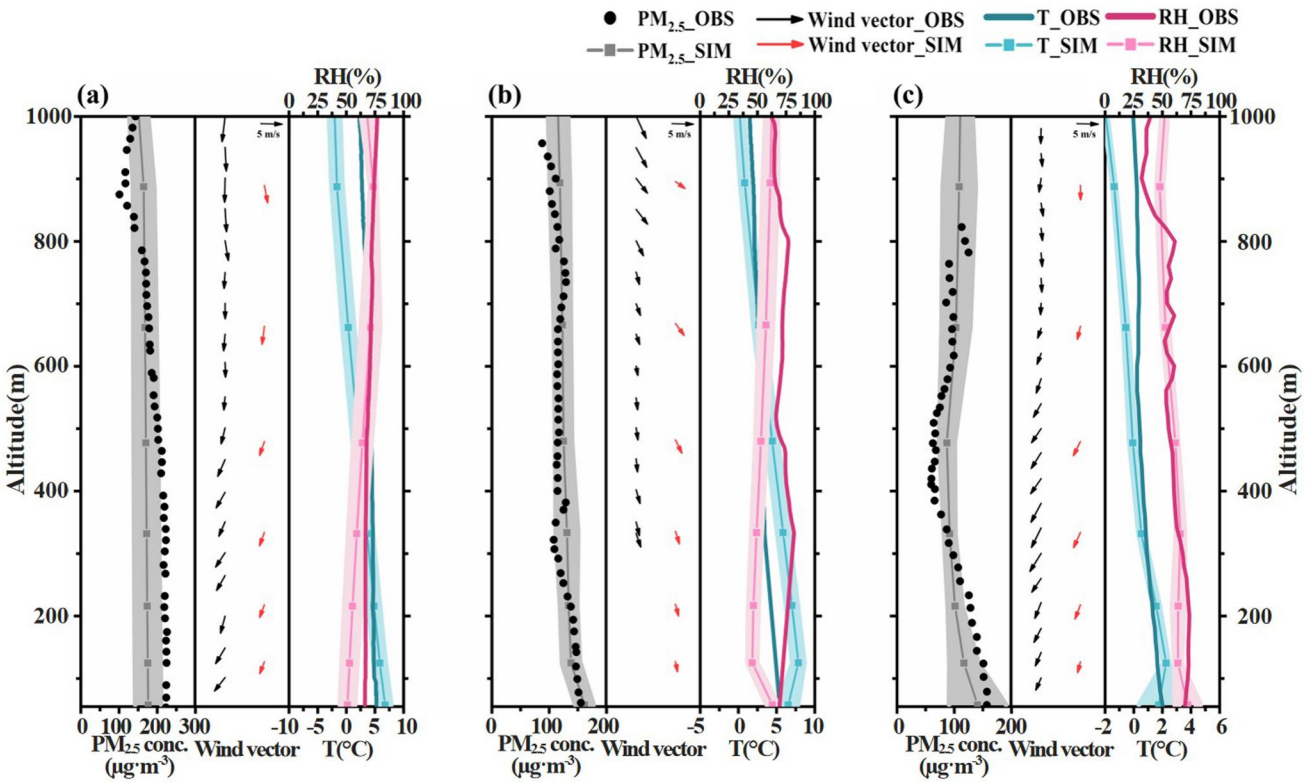

Figure 3. Vertical distribution of observed and simulated $PM_{2.5}$ mass concentration and meteorological parameters in Nanjing at (a) 12:00 LT 15 January, (b) 20:00 LT 19 January, and (c) 08:00 LT 20 January.

SNA contributing 63.0% of $PM_{2.5}$ mass concentrations. The model simulation results were satisfactory because the model successfully replicates the diurnal variation of pollutant concentrations. The correlation coefficients for $PM_{2.5}$, SO_4^{2-}, NO_3^-, and NH_4^+ were found to be 0.74, 0.58, 0.83, and 0.80, respectively, and passed the significance test of $P < 0.01$.

To further validate the model performance, some statistical metrics, including the correlation coefficient (R), normalized mean bias (NMB), and normalized mean error (NME), were calculated to compare simulated results

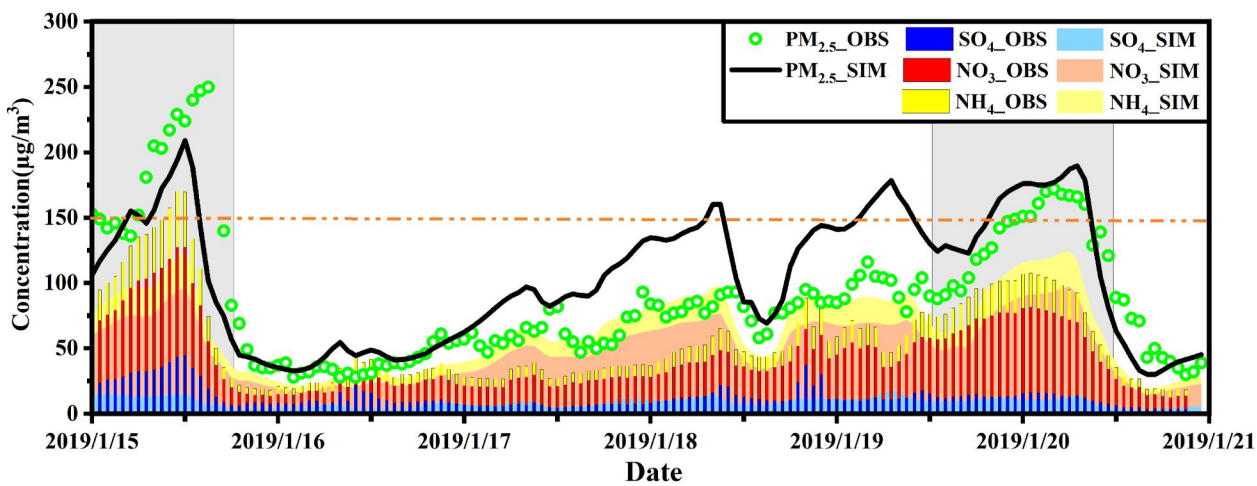

Figure 4. Time series of observed and simulated $PM_{2.5}$ and its major chemical composition (SO_4^{2-}, NO_3^-, and NH_4^+) mass concentration from 00:00 LT 15 January 2019 to 00:00 LT 20 January 2019 at Nanjing. (The gray shadows indicate the two cold front episodes considered in this study.)

Table 1
Statistical Test Results of $PM_{2.5}$, SO_2 and NO_2 Mass Concentration and Meteorological Elements (Temperature, Wind Speed, Wind Direction, and Relative Humidity)

	Beijing			Huaian			Nanjing		
	R	NMB	NME	R	NMB	NME	R	NMB	NME
$PM_{2.5}$	0.80	−8.0%	35.6%	0.81	−6.7%	26.4%	0.74	−7.86%	27.8%
T	0.86	10.5%	−119.6%	0.95	57.3%	80.8%	0.88	3.2%	35.7%
RH	0.41	27.8%	48.6%	0.73	−20.4%	22.6%	0.62	−17.6%	21.2%
Wspd	0.68	−26.2%	46.1%	0.78	31.9%	49.6%	0.67	37.3%	50.6%
Wdir	0.88	−2.7%	13.1%	0.96	2.8%	11.9%	0.93	−1.4%	16.8%
SO_2	0.76	43.3	43.8	0.46	51.5	59.3	0.40	36.1	42.7
NO_2	0.89	−46.2	46.2	0.72	11.9	30.2	0.74	9.1	34.1

with observations for $PM_{2.5}$, SO_2 and NO_2 concentration and meteorological elements (temperature, wind speed, wind direction, and relative humidity) separately (Table 1). Statistical metrics were calculated as follows:

$$R = \frac{Cov(x,y)}{\sqrt{D(x)}\sqrt{D(y)}} \tag{1}$$

$$NMB = \frac{\sum_{i=1}^{N}(M_i - O_i)}{\sum_{i=1}^{N} O_i} \times 100\% \tag{2}$$

$$NME = \frac{\sum_{i=1}^{N}|M_i - O_i|}{\sum_{i=1}^{N} O_i} \times 100\% \tag{3}$$

where M_i are the hourly model simulations, O_i are the hourly observations, and N denotes the number of data pairs.

The correlation coefficients for $PM_{2.5}$ concentrations were above 0.74 for all assessed sites (Table 1). Regarding the meteorological factors, the correlation coefficients were higher than 0.62 for all sites except for the relative humidity at Beijing, and for temperature and wind direction were found to be around 0.90 for all sites. Overall, simulations of all variables exhibit well agreement with the observations, confirming that the model simulations reasonably captured the 3-D and temporal variations of meteorological variables, and $PM_{2.5}$ concentration over east China, and surface SNA concentrations in Nanjing during the pollution period. Even if the model accurately replicates the variation in pollutant concentration, biases still exist. These biases can be related to the bias in the meteorological simulation, the substantial uncertainty in the emission inventory, the relatively coarse grid size of the model, and the incomplete consideration of the atmospheric chemical processes (Harris et al., 2013).

3.2. Synoptic Situations and Air Pollution Events

Figure 5 displays the time-latitude distribution of observed $PM_{2.5}$ concentrations, wind vectors, and 24-hr temperature changed from 14 January 2019–21 January 2019 at 14 cities (connected by a solid black line in Figure 1) spanning from the NCP to the YRD. Two heavy pollution episodes occurred in eastern China during this period: on 15-16 January (defined as episode 1) and 19-20 January (defined as episode 2) respectively, both due to the transport of high concentrations of $PM_{2.5}$ from north to south under the influence of cold fronts. The high-value area of $PM_{2.5}$ concentrations and time series showed a belt distribution from north to south, characterized by the significant short-term variation of pollution events and meteorological elements, strong northerly winds near the surface, and sharp temperature decreases. There is a distinct difference between the transport paths of the air mass in the two cold front episodes.

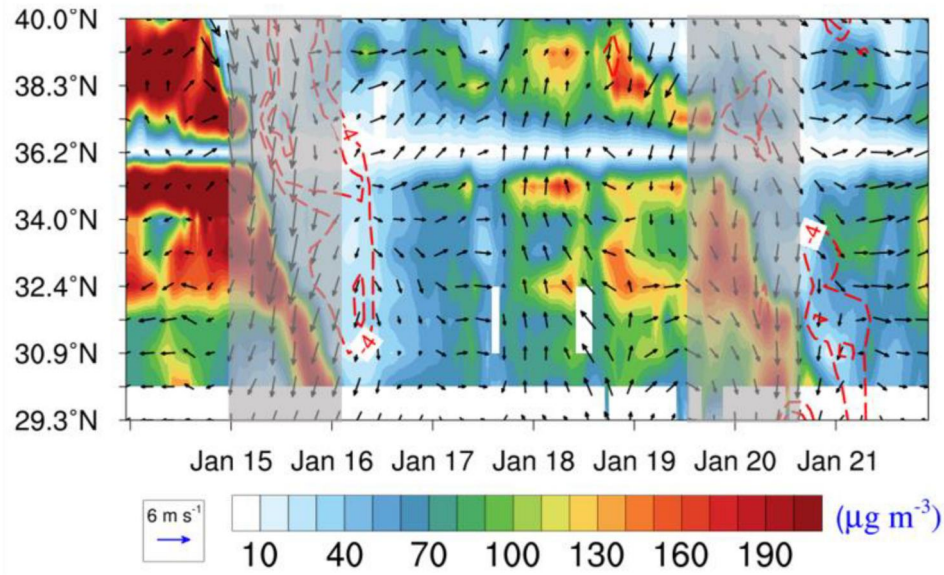

Figure 5. Surface $PM_{2.5}$ concentrations (color-filled contours), wind vectors, and 24-hr temperature changes (dashed red lines) at 14 cities (connected by solid black line in Figure 1) from the north of the North China Plain (NCP) to the south of the Yangtze River Delta (YRD) from 00:00 LT 14 January 2019 to 00:00 LT 21 January 2019. The white area denotes missing values. The gray shadows indicate the two cold front episodes considered in this study.

According to the backward trajectory (72 hr) of air masses calculated by the HYSPLIT model, the surface air mass moved southly along the northwest path from the NCP to the YRD in episode 1 (Figure 6b). The cold air was strong and moved fast, and the pollution level was heavier (Figures 5 and 6e), which is the most common pollution type in winter (Liu et al., 2021). In episode 2, the near-surface air mass originated from Anhui (AH) and the YRD, then moved to the NCP and eventually turned southward into the YRD along the northeast path (Figure 6d). The cold air was relatively weak, with a less common pollution type during autumn and winter in eastern China (Liu et al., 2021). The backward trajectory model results are consistent with the source-tracing results. Source apportionment of $PM_{2.5}$ and SNA was further investigated in detail in Section 3.3.

Figure 6 further revealed the synoptic situations and presented the simulated $PM_{2.5}$ distribution for the two episodes. In EP1, the center of the Siberian high-pressure system was located over west of Lake Baikal on 15 January. By 02:00 LT, the cold front in front of the high pressure initially arrived in southern NCP. At the same time, the YRD was controlled by the uniform-pressure field in front of the high pressure, resulting in adverse atmospheric dispersion conditions (Figure 6a). Shandong, western and central Anhui, and Jiangsu suffered a severe air pollution (Figure 6e). Thereafter, the center of high pressure strengthened. At 11:00 LT 15 January (Figure 6b), $PM_{2.5}$ concentrations significantly decreased in southern Hebei and most of Shandong due to northerly winds with clean air behind the cold front. As the shown in Figure 5, the $PM_{2.5}$ high-value area moved southly along the northwest path (Figure 6f). Comparatively, in EP2, the center of the Siberian high-pressure system was located southwest of Lake Baikal at 20:00 LT on 19 January (Figure 6c). The cold air moved southly along the northeast path. Shandong was mainly influenced by eastern airflow, and the overall air pollution level was relatively low (Figure 6g). The isobars became denser in the YRD at 05:00 LT on 20 January (Figures 6d and 6h). The analysis mentioned above demonstrates that the two episodes are representative of the impact on the long-range transport of $PM_{2.5}$ to downstream regions by winter cold fronts, as described by Liu et al. (2021). The distribution and evolution of the SNA, as well as the formation processes and mechanisms under the influence of the 2 types of cold fronts are discussed further below.

3.3. Source Apportionment of $PM_{2.5}$ and SNA During Cold Frontal Events

The time series of contributions of source regions to $PM_{2.5}$ and SNA concentrations in the YRD are shown in Figure 7. The difference between the transport routes in the two cold front episodes is discussed in Section 2. The source-tracing results (Figure 7a) show that in EP1, the cold front effectively transported $PM_{2.5}$ and SNA from the

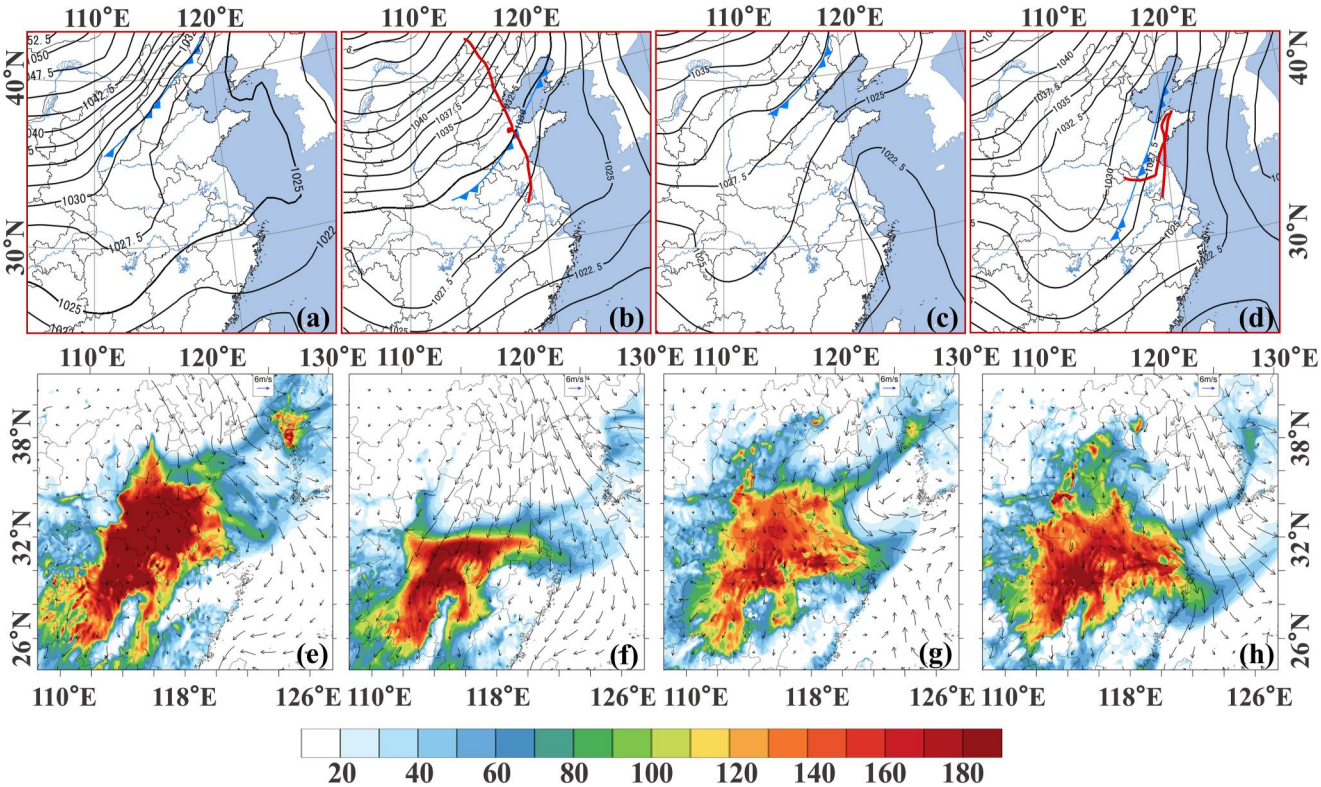

Figure 6. (a)–(d) Surface weather patterns over eastern Asia and (e)–(h) simulated $PM_{2.5}$ mass concentrations (color-filled contours) with wind vectors (arrows) at ground level at (a) and (e) EP1: 02:00LT on 15 January, (b) and (f) EP1: 11:00LT on 15 January, (c) and (g) EP2: 20:00LT on 19 January, (d) and (h) EP2: 05:00LT on 20 January. (b) and (d) Backward trajectory (24 hr) of the air mass reaches 500 m above Nanjing (red line). The blue lines with blue triangles indicate the heads of cold fronts.

NCP to the downstream YRD. The near-surface $PM_{2.5}$ contribution from the NCP (31.4%) was comparable to that from the YRD (35.5%). In EP2, the cold front was weaker than in EP1 and the YRD was mainly affected by the joint contribution of the NCP and AH. The local contribution of YRD itself accounted for 36.8%, and the contributions from the upstream sources mostly came from NCP (18.0%) and AH (14.6%). In the non-cold front period, local and upstream sources contributions were approximately 44.6% (~10% higher than during cold front periods) and 18.8% (~12% lower than during cold front periods). The contributions of $PM_{2.5}$ sources in the two cold front episodes were consistent with the backward trajectory results in Figures 6b and 6d. As shown in Figures 8a and 8e, upstream sources contributed 37.5%–41.0% in the upper boundary layer (BL) (0.5–1.0 km) (~15% higher than during non-cold front periods). The long-range transport from the external sources (including the upstream, southwest of YRD (SWY), BCIC, and OTHR regions) contributed about 90.4%–91.8% in the lower free troposphere (LFT) (1.0–2.0 km). Local contribution from the YRD decreased from 21.2% to 23.2% in the upper BL to 8.2%–9.6% in the LFT. The local source contribution in EP2 was relatively higher than in EP1 as the air mass hovered, and the upstream sources contribution was lower than in EP1. Despite the distinct transport paths of the two cold front episodes, the variation and vertical structure of the source apportionment during the two episodes had commonalities, primarily affected by long-range transport from upstream regions. The results of the two episodes will be combined for the analysis below.

$(NH_4)_2SO_4$ is influenced by the gas-particle equilibrium as well as the vapor-liquid equilibrium on the aerosol surface when atmospheric RH is relatively high. $(NH_4)_2SO_4$ mostly exists as particle phase in the air and is difficult to dissociate into gas phase due to the dissociation constants of ammonium sulfate aerosol are very small and with weak variable at different heights and temperatures in the air. In Figure 7b, the contributions of local source on SO_4^{2-} in the two cold front events near the surface were 26.9% and 31.2%, respectively, while upstream sources predominantly contributed 43.7%–53.1%. The time-weighted average (TWA) contribution of upstream sources and the YRD for two episodes near the surface were 48% and 29%, respectively (Table 2). In contrast, in

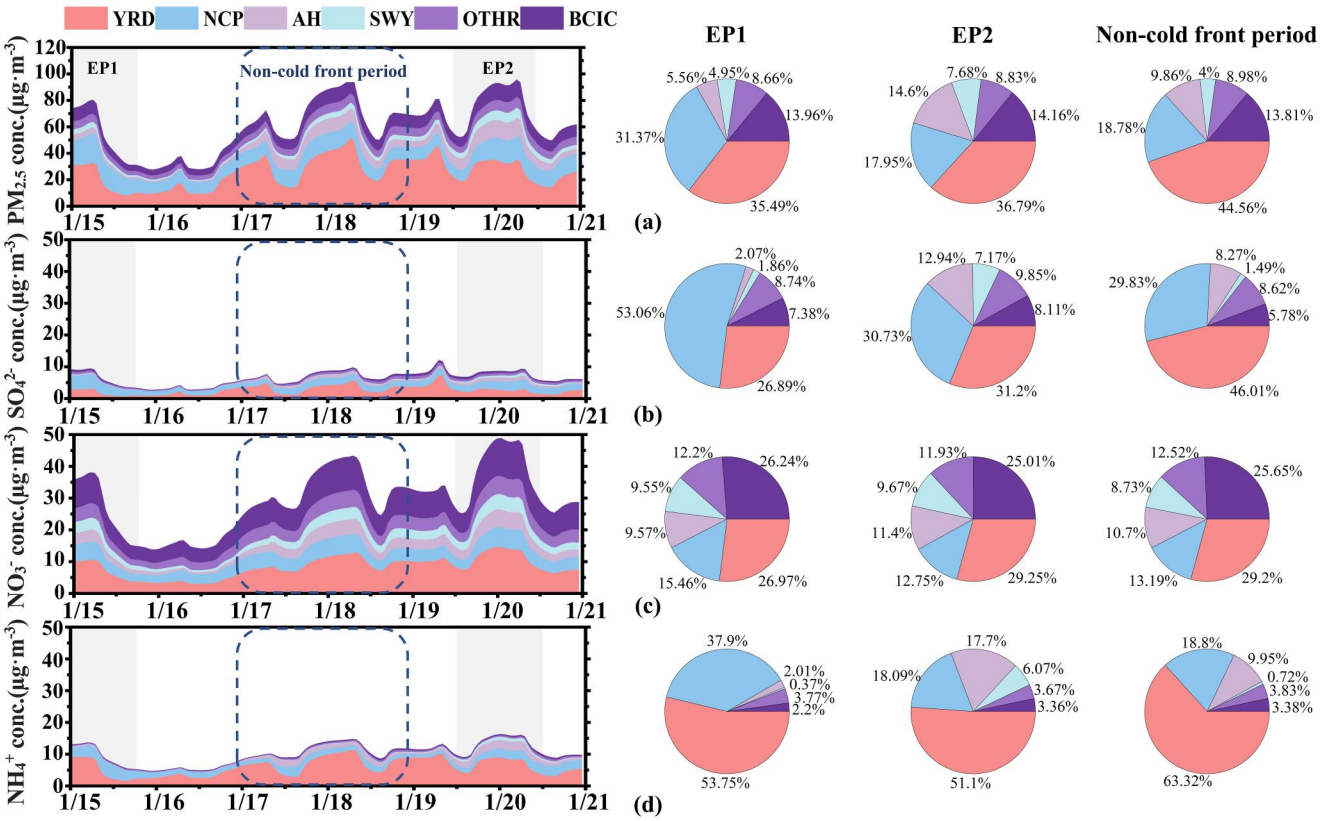

Figure 7. Surface (a) $PM_{2.5}$, (b) SO_4^{2-}, (c) NO_3^-, and (d) NH_4^+ concentration of each source region over the YRD from 00:00 LT 15 January 2019 to 00:00 LT 20 January 2019. The pies from left to right denote the surface mean contribution over the YRD during EP1, EP2 and the non-cold front period, respectively. The legend refers to the regions shown in Figure 1. (The gray shadows and blue dashed box indicate the two cold front episodes and non-cold front period considered in this study.)

the non-cold front period (Figure 7b), local and upstream source contributions were approximately 46.0% (~18% higher than that of the cold front period) and 29.8% (~20% lower than that of the cold front period), respectively. As illustrated in Figures 8b and 8f, the contribution from long-range transport become dominant as altitude increased, with about 44.9%–53.3% contribution from the upstream sources in the upper BL (TWA contribution was 49% higher than the non-cold front period 14%), only 13.7%-21.6% contribution from local source (TWA contribution was 18% lower than the non-cold front period 9%). The local contribution in the LFT was below 6%, and the rest was contributed by external sources.

The gas-particle and the vapor-liquid equilibrium on the aerosol surface in the relatively high RH condition have a joint impact on NH_4NO_3. Compared with $(NH_4)_2SO_4$, the dissociations of ammonium nitrate aerosol strongly depend on air temperature. NH_4NO_3 is temperature-sensitive, thermally unstable, and readily dissociated in the warmer and lower BL. At high elevations where the air is colder, the balance is on the side of the particle phase, and NH_4NO_3 is quite stable and difficult to dissociate into the gas phase (Seinfeld & Pandis, 1998). Driven by cold front, the vertical advection and diffusion lift the prefrontal warm moist air mass to the upper BL and LFT, and the cold environment leads to more NH_4NO_3 formation. Kang et al. (2022) revealed that urban heat island circulation causes similar high-altitude NH_4NO_3 formation. Since the deposition velocities of HNO_3(g) are significantly greater than those of nitrate (about one order of magnitude) (Zhai et al., 2021), total nitrate ($NO_3^T \equiv HNO_3 + NO_3^-$) is rapidly lost near the surface due to repeated gas-particle thermodynamic conversion and dry deposition effects. Hence, NO_3^- was more easily lost than SO_4^{2-} in the lower BL. In Figure 7c, the upstream sources of NO_3^- was 15.5%–24.2% of the total NO_3^- near the surface, much lower than that of SO_4^{2-} (TWA contribution was 27% lower than SO_4^{2-}). However, the local source contributions of NO_3^- and SO_4^{2-} were similar (around 28%) due to rapid mixing in the BL (Table 2). We can also find that there was no distinct difference of NO_3^- source ratios in the cold front and non-cold front periods, might indicating NO_3^- was mainly controlled by local sources and atmospheric mixing around the surroundings. As altitude increases and

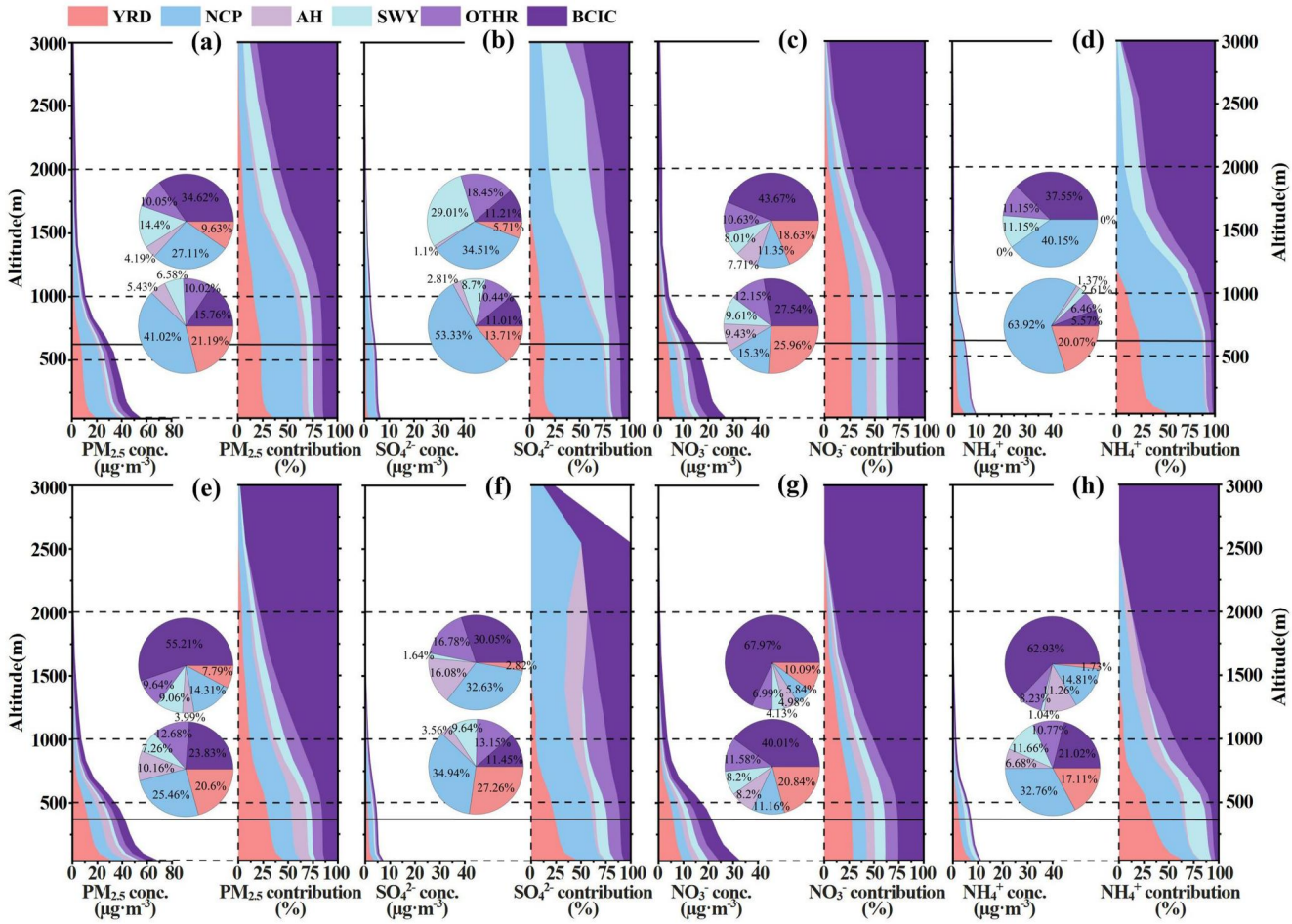

Figure 8. Averaged vertical distributions of (a) and (e) $PM_{2.5}$, (b) and (f) SO_4^{2-}, (c) and (g) NO_3^-, and (d) and (h) NH_4^+ concentration and contribution ratio of each source region in the YRD during (a)–(d) EP1 and (e)–(h) the non-cold front period. The bottom up pies denote the mean contribution at 0.5–1.0, and 1.0–2.0 km over the YRD. The black solid lines denote the average boundary layer height. The legend refers to the regions shown in Figure 1.

temperature decreases, NH_4NO_3 stabilizes intensely and has a longer lifetime than near the surface. In the upper BL, the local sources - contributed about 26.0%–27.8% of NO_3 (TWA contribution was 9% higher than SO_4^{2-} and 6% lower than the non-cold front period), whereas upstream sources contributed 15.3%–23.7% (TWA contribution was 27% lower than SO_4^{2-} and 9% higher than the non-cold front period). In the LFT, the contribution from the local source of NO_3^- was about 18.6% (~13% higher than SO_4^{2-} and 9% higher than the non-cold front period), while the contribution from the external source was around 81.4% (~13%–17% lower than SO_4^{2-} and 9% lower than the non-cold front period). Considering the temperature sensitivity of NH_4NO_3, the lifetime differences between NH_4NO_3 and $(NH_4)_2SO_4$, and the cold front physical effects, we can explain why NO_3^- is dominant by local source compared to SO_4^{2-} in the BL and LFT, as well as the slighter concentration gradient in the vertical distribution compared to SO_4^{2-} in (Figure 8).

Table 2
SO_4^{2-} and NO_3^- Averaged Contribution Ratio From the Upstream Sources and YRD Sources to YRD During EP1, EP2 and Time-Weighted Average (TWA) Contribution Ratios for Two Episodes Near the Surface and Within 0.5–1.0 km

		Surface			0.5–1.0 km		
	Source	EP1	EP2	TWA	EP1	EP2	TWA
SO_4^{2-}	Upstream	53.1%	43.7%	47.7%	53.3%	44.9%	48.5%
NO_3^-		15.5%	24.2%	20.4%	15.3%	23.7%	20.1%
SO_4^{2-}	YRD	26.9%	31.2%	29.3%	13.7%	21.6%	18.2%
NO_3^-		27.0%	29.3%	28.3%	26.0%	27.8%	27.0%

NH_4^+ was jointly affected by SO_4^{2-} and NO_3^-, and its upstream sources contribution ratio was between SO_4^{2-} and NO_3^- near the surface. The contribution from local source was greater than that from the upstream sources. The local contribution near the surface was higher than 50% for the two cold front episodes, and the upstream sources contributed 35.8%–37.9% (Figure 7d). In contrast, in the non-cold front period, the local contribution was around 63.3%, and the NCP contribution was about 18.8%. The average

upstream sources contribution reached 60.3%–63.9% in the upper BL (~29% higher than that of the non-cold front period), and the local YRD contribution was only 16.7%–20.0% (similar to the non-cold front period) (Figures 8d and h). There was almost no local YRD contribution in the LFT. The mechanism of physical and chemical processes influencing the formation and distribution of SNA will be further elaborated in Section 3.4 by process analysis.

3.4. The Physical and Chemical Processes of SNA Evolution

In this section, the process analysis technique was used to further investigate how cold fronts affect the vertical distribution of $PM_{2.5}$ and SNA through accounting each physical and chemical processes (Figure 9). Cold fronts transported polluted air masses from upstream areas (e.g., NCP, AH, etc.) to the YRD through the horizontal advection (HADV) process, increasing the inflow of $PM_{2.5}$ into the atmosphere within 0–2 km. The HADV process removed pollutants rapidly when the cold front moved through. The vertical advection (ZADV) process negatively contributed to the $PM_{2.5}$ concentration below 500 m but was positive above 500 m, which indicated that the ZADV process driven by cold fronts transported the warm, moist, and polluted air mass with high $PM_{2.5}$ concentrations from the lower BL to the upper BL and LFT. The vertical diffusion (VDIF) process mixed the $PM_{2.5}$ near the surface with the upper air. The VDIF process had a significantly negative contribution to $PM_{2.5}$ near the surface since the emissions of $PM_{2.5}$ and its precursors therein. The VDIF process contributed positively to the upper BL, indicating that the VDIF process diffused aerosol and its precursors from the surface to the upper air through turbulent mixing. Physical processes had relatively consistent effects on variations in $PM_{2.5}$ and SNA concentrations.

Ammonium sulfate was highly thermally stable and impervious to dissociation, and its dissociation constant varied slightly at different heights and temperatures in the air. Thus, the chemical process always contributed positively, peaking near 1.5 km above the surface (Figure 9b). Comparatively, NH_4NO_3 was thermally unstable and in a reversible equilibrium of dissociation/condensation at high/low temperatures. As shown in Figure 9c, when the cold front reached the YRD at 06:00 LT on 15 January, abundant SNA and gas precursors from the upstream and local regions formed high concentrations of SNA near the surface, showing a positive contribution in the AERO process. The ZADV and VDIF processes driven by the cold front forced the warm and humid air mass lifting upward in front of the cold front zone (Kang et al., 2021). We can see NH_4NO_3 dissociated at 500 m due to relative high temperature (>0°C). At around 900 m above the surface, the equilibrium shifted to the aerosol phase at lower temperature (<0°C) and high aerosol water content, which promoted the condensation of ammonium nitrate therein. Under the effect of uplifting and mixing, the temperature-sensitive and thermally unstable NH_4NO_3 repeatedly dissociated/condensated, and HNO_3 effectively deposited near the surface, resulting in the AERO process contributing positively in the upper BL and negatively in the lower BL.

4. Conclusions

Because of the distinct thermostability and lifetime difference between ammonium sulfate and ammonium nitrate aerosols, coupled with variations in SNA emissions and precursors across different regions, the distributions, variations and sources of SNA are complex and unpredictable under the long-range transport conditions with sharply changed meteorology. Focusing on these issues, this study investigated the regional sources, 3-D structures and formation mechanisms of physical and chemical processes of $PM_{2.5}$ and SNA during two cold front episodes, utilizing the CMAQ model with an online source apportionment module, combined with the field experiments conducted in situ to monitor boundary layer air pollution and meteorology. The major findings are summarized as follows:

Observations showed a southward movement of the peaks of $PM_{2.5}$ along the cold frontal passages and effectively transported $PM_{2.5}$ from the NCP to the YRD, which was well captured by the model simulations. Also, the model reasonably reappeared the 3-D structures and temporal variations of meteorological elements, $PM_{2.5}$ and the surface SNA concentrations. Model simulations reveal that cold front can effectively uplift and transport the upstream sources of $PM_{2.5}$ and its precursors to the YRD. Specifically, near the BL of YRD, SO_4^{2-} was mostly imported from the upstream sources, around 48% (time-weighted average of 2 episodes) near the surface, much higher than from local source (~29%). In contrast to $(NH_4)_2SO_4$, NH_4NO_3 is thermally unstable and readily dissociated in the warmer lower BL. Under repeated gas-particle thermodynamic conversion and dry deposition effects, NO_3^- was more easily lost than SO_4^{2-} in the lower BL. Therefore, the upstream sources of NO_3^- was

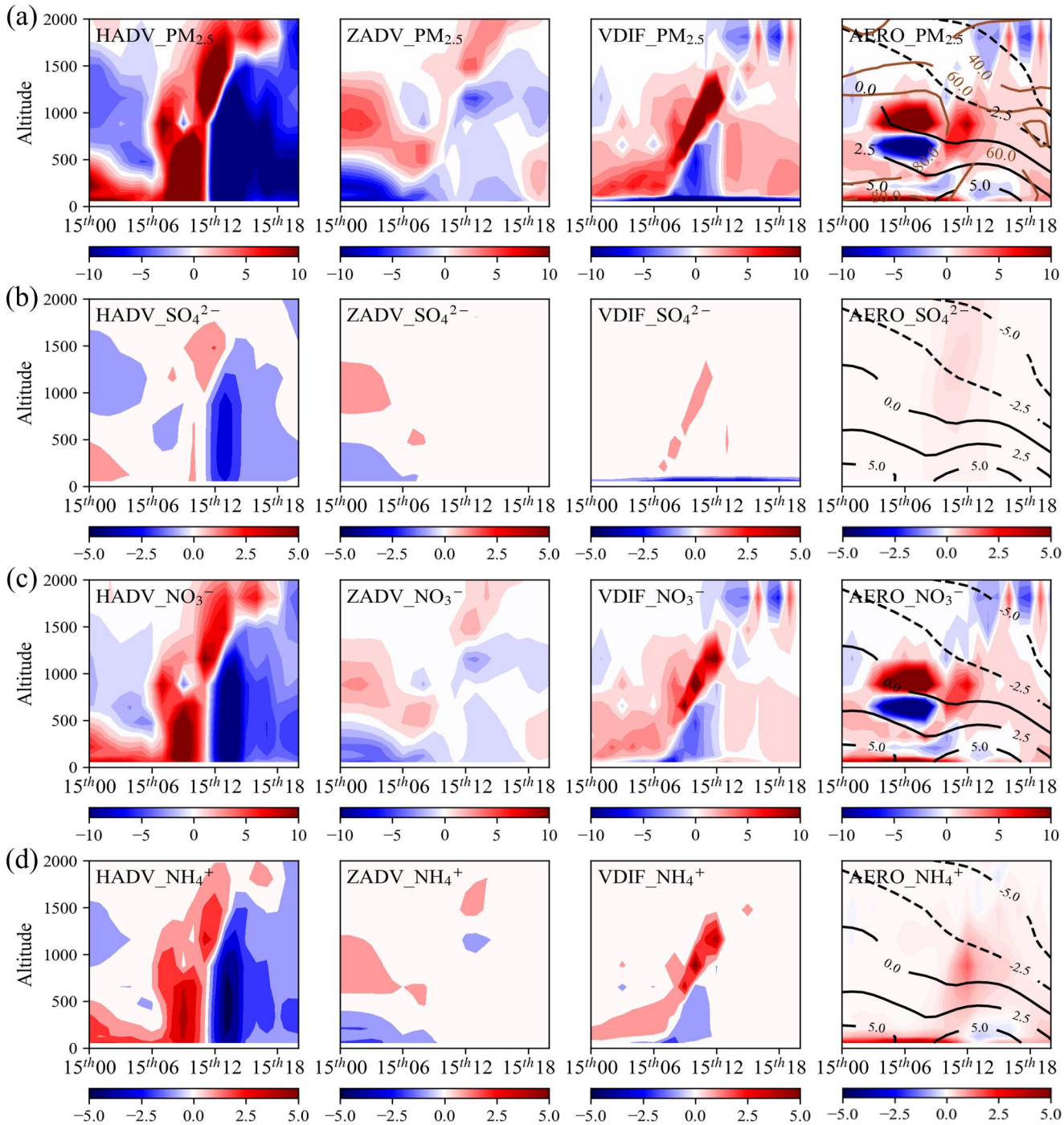

Figure 9. Vertical contributions of horizontal advection (HADV), vertical advection (VADV), vertical mixing (VMIX), and aerosol processes (AERO) to (a) $PM_{2.5}$, (b) SO_4^{2-}, (c) NO_3^- and (d) NH_4^+ in Nanjing during EP1. The black and brown lines in AERO process panels represent air temperature (°C) and RH (%) respectively.

only 20% of the total NO_3^-, much lower than that of SO_4^{2-}, and the local source contributed 28% of NO_3^- near the surface.

In the upper BL, the contribution of SO_4^{2-} from the long-range transport to the YRD was still high, with about 49% from the upstream sources but only 18% from local source. In the LFT, the local contribution was below 6%, and the contribution from the external sources varied between 94% and 98%. In contrast, NH_4NO_3 stabilized intensely and had a longer lifetime in the cold and wet upper BL with high aerosol water content. Local source of

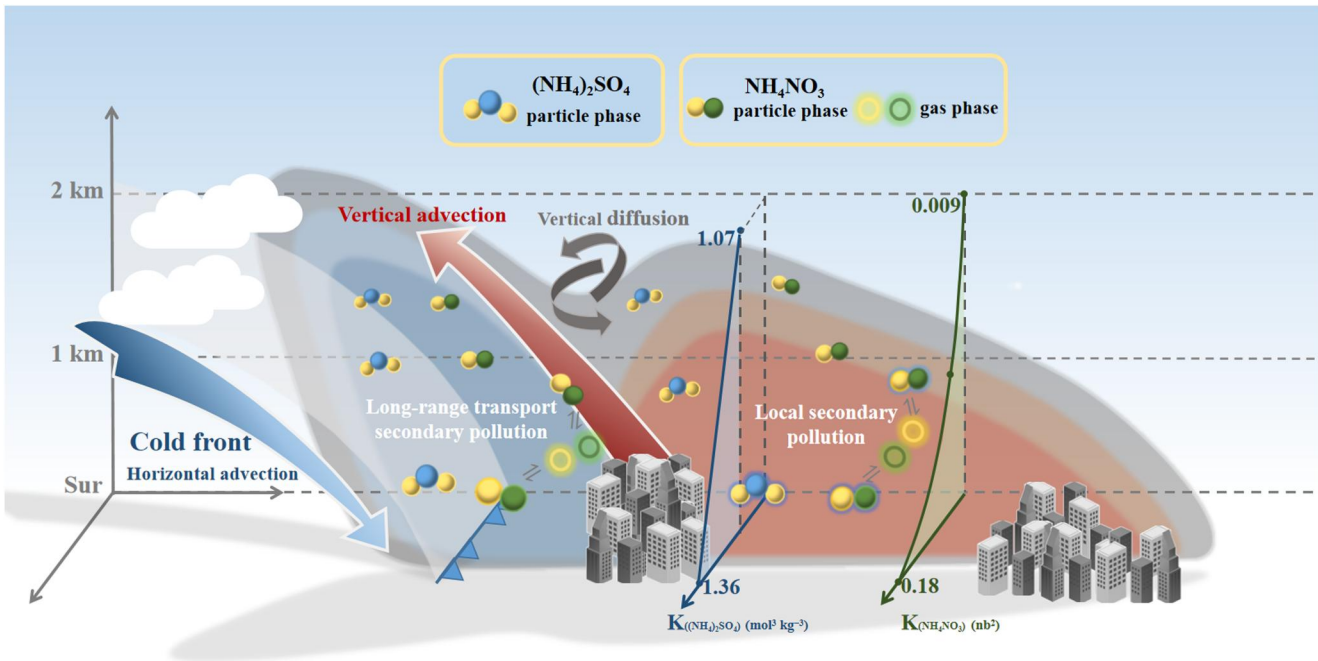

Figure 10. A conceptual scheme for the three-dimensional structures and sources of sulfate ammonium and nitrate ammonium aerosols during cold front episodes. The hollow yellow and green dots denote NH_3(g) and HNO_3(g). The blue, green, and yellow dots indicate SO_4^{2-}, NO_3^-, and NH_4^+, respectively. The size of the dot represents the particle concentrations and the blue shadow on the dot represents high aerosol water content. The blue and green vertical profiles indicate the variation of dissociation constants of $(NH_4)_2SO_4$ and NH_4NO_3 with height. The cold front (the blue arrow) transports polluted cold air masses (the blue shadow) from the upstream region to the downstream region through the horizontal advection process. The vertical advection and diffusion processes (the red arrow and grep rotation arrows) driven by the cold front forced the local warm and humid air masses (the red shadow) to lift upward in front of the cold front zone. Under drastic changes in meteorological conditions, compared to $(NH_4)_2SO_4$, NH_4NO_3 was temperature-sensitive and in an obvious reversible equilibrium of dissociation/condensation at high/low temperatures.

NO_3^- contributed 27%, whereas upstream sources contributed 20%. In the LFT, the local source contribution to NO_3^- was about 19%, much higher than that of SO_4^2.

NH_4^+ was jointly affected by SO_4^{2-} and NO_3^-, with local and upstream sources contributing 52% and 37%, respectively, near the surface. The average upstream sources contribution to NH_4^+ increased to 62% in the upper BL, and the local YRD contribution was only 19%, and negligible local contribution to NH_4^+ in the LFT.

Physical processes had relatively consistent effects on variations in $PM_{2.5}$ and SNA concentrations. The $PM_{2.5}$ chemical (AERO) process formed a greater mass concentration of NH_4NO_3 than $(NH_4)_2SO_4$. The AERO process of $(NH_4)_2SO_4$ consistently contributed positively in the whole BL, peaking near 1.5 km. Comparatively, under the uplifting and mixing effects, the temperature-sensitive NH_4NO_3 repeatedly dissociated/condensated, and HNO_3 deposited near the surface, resulting in positive AERO process contributions in the upper BL and negative contributions in the lower BL.

At last, we propose a conceptual framework to demonstrate the complex mechanisms controlling the three-dimensional structures and sources of $(NH_4)_2SO_4$ and NH_4NO_3 due to their thermostability and lifetime differences under a long-range transport condition (Figure 10). Compared to highly thermally stable $(NH_4)_2SO_4$, NH_4NO_3 has unique properties, that is, being thermally unstable in the warmer lower BL but quite stable in the cold and wet upper air. Under drastic changes in meteorological conditions caused by the cold front passages, NH_4NO_3 was in a reversible equilibrium of dissociation/condensation at high/low temperatures and was dominant by local source. In contrast, $(NH_4)_2SO_4$ was impacted by the upstream significantly. These results indicate that one difference in the physicochemical properties of air species can lead to distinct distributions and sources on a large scale, especially under long-range transport conditions. This insight underscores the importance of considering these differences in regional air pollution control strategies.

Data Availability Statement

All data used during this study are openly available. The MEIC anthropogenic emission data were acquired from http://meicmodel.org/ (Li et al., 2017). The reanalysis meteorological parameters data are available at National Centers for Environmental Prediction/National Weather Service/NOAA/U.S. Department of Commerce (2015). The HYSPLIT transport and dispersion model were available at https://www.ready.noaa.gov/ (Rolph et al., 2017; Stein et al., 2015). The vertical profiles of meteorological parameters and $PM_{2.5}$ concentrations in the boundary layer and ground-based SNA online observations in the northern suburb of Nanjing City are publicly available at Peng (2024).

Acknowledgments
This work is financially supported by the National Natural Science Foundation of China (42021004, 42275115). The numerical calculations in this paper have been done on the high-performance computing system in the High-Performance Computing Center, Nanjing University of Information Science and Technology. The authors gratefully acknowledge the NOAA Air Resources Laboratory (ARL) for the provision of the HYSPLIT transport and dispersion model and/or READY website (https://www.ready.noaa.gov) used in this publication. We sincerely appreciate all valuable comments and suggestions from the 2 reviewers, which help us to improve the quality of the manuscript.

References

Appel, K. W., Bash, J. O., Fahey, K. M., Foley, K. M., Gilliam, R. C., Hogrefe, C., et al. (2021). The Community Multiscale Air Quality (CMAQ) model versions 5.3 and 5.3.1: System updates and evaluation. *Geoscientific Model Development*, *14*(5), 2867–2897. https://doi.org/10.5194/gmd-14-2867-2021

Byun, D. W., & Ching, J. (1999). Science algorithms of the EPA Models-3 Community Multiscale Air Quality (CMAQ) Modeling System. *Nerl*. https://api.semanticscholar.org/CorpusID:128521998

Ding, A., Huang, X., Nie, W., Chi, X., Xu, Z., Zheng, L., et al. (2019). Significant reduction of $PM_{2.5}$ in eastern China due to regional-scale emission control: Evidence from SORPES in 2011–2018. *Atmospheric Chemistry and Physics*, *18*, 11791–11801. https://doi.org/10.5194/acp-19-11791-2019

Fan, Z., Wang, Z. W., Cheng, H. R., Lv, X. P., Wei, G., Wang, X. M., & Zhang, G. (2015). Seasonal variations and chemical characteristics of $PM_{2.5}$ in Wuhan, central China. *Science of the Total Environment*, *518–519*(jun.15), 97–105. https://doi.org/10.1016/j.scitotenv.2015.02.054

Ge, B., Xu, X., Ma, Z., Pan, X., Wang, Z., Lin, W., et al. (2019). Role of ammonia on the feedback between AWC and inorganic aerosol formation during heavy pollution in the North China Plain. *Earth and Space Science*, *6*(9), 1675–1693. https://doi.org/10.1029/2019EA000799

Griffith, S. M., Huang, X., Louie, P., & Yu, J. Z. (2015). Characterizing the thermodynamic and chemical composition factors controlling $PM_{2.5}$ nitrate: Insights gained from two years of online measurements in Hong Kong. *Atmospheric Environment*, *122*(DEC), 864–875. https://doi.org/10.1016/j.atmosenv.2015.02.009

Guenther, A. B., Jiang, X., Heald, C. L., Sakulyanontvittaya, T., Duhl, T., Emmons, L. K., & Wang, X. (2012). The Model of Emissions of Gases and Aerosols from Nature version 2.1 (MEGAN2.1): An extended and updated framework for modeling biogenic emissions. *Geoscientific Model Development*, *5*(6), 1471–1492. https://doi.org/10.5194/gmd-5-1471-2012

Guo, S., Hu, M., Zamora, M. L., Peng, J. F., Shang, D. J., Zheng, J., et al. (2014). Elucidating severe urban haze formation in China. *Proceedings of the National Academy of Sciences of the United States of AmericaProceedings of the National Academy of Sciences of the United States of AmericaProceedings of the National Academy of Sciences of the United States of America*, *111*(49), 17373–17378. https://doi.org/10.1073/pnas.1419604111

Harris, E., Sinha, B., Pinxteren, D. v., Tilgner, A., Fomba, K. W., Schneider, J., et al. (2013). Enhanced role of transition metal ion catalysis during in-cloud oxidation of SO_2. *Science*, *340*(6133), 727–730. https://doi.org/10.1126/science.1230911

Hu, M., Wu, Z., Slanina, J., Lin, P., Liu, S., & Zeng, L. (2008). Acidic gases, ammonia and water-soluble ions in $PM_{2.5}$ at a coastal site in the Pearl River Delta, China. *Atmospheric Environment*, *42*(25), 6310–6320. https://doi.org/10.1016/j.atmosenv.2008.02.015

Huang, X., Ding, A., Wang, Z., Ding, K., Gao, J., Chai, F., & Fu, C. (2020). Amplified transboundary transport of haze by aerosol–boundary layer interaction in China. *Nature Geoscience*, *13*(6), 428–434. https://doi.org/10.1038/s41561-020-0583-4

Janjić, Z. I. (1994). The step-mountain eta coordinate model: Further Developments of the convection, viscous sublayer, and turbulence closure schemes. *Monthly Weather Review*, *122*(5), 927–945. https://doi.org/10.1175/1520-0493(1994)122<0927:Tsmecm>2.0.Co;2

Kang, H., Zhu, B., de Leeuw, G., Yu, B., vander Ronald, A. J., & Lu, W. (2022). Impact of urban heat island on inorganic aerosol in the lower free troposphere: A case study in Hangzhou, China. *Atmospheric Chemistry and Physics*, *22*(16), 10623–10634. https://doi.org/10.5194/acp-22-10623-2022

Kang, H., Zhu, B., Gao, J., He, Y., Wang, H., Su, J., et al. (2019). Potential impacts of cold frontal passage on air quality over the Yangtze River Delta, China. *Atmospheric Chemistry and Physics*, *19*(6), 3673–3685. https://doi.org/10.5194/acp-19-3673-2019

Kang, H., Zhu, B., Liu, X., Shi, S., Hou, X., Lu, W., et al. (2021). Three-dimensional distribution of $PM_{2.5}$ over the Yangtze River Delta as cold fronts moving through. *Journal of Geophysical Research: Atmospheres*, *126*(8), e2020JD034035. https://doi.org/10.1029/2020JD034035

Kwok, R. H. F., Napelenok, S. L., & Baker, K. R. (2013). Implementation and evaluation of $PM_{2.5}$ source contribution analysis in a photochemical model. *Atmospheric Environment*, *80*, 398–407. https://doi.org/10.1016/j.atmosenv.2013.08.017

Lamarque, J. F., Emmons, L. K., Hess, P. G., Kinnison, D. E., Tilmes, S., Vitt, F., et al. (2012). CAM-chem: Description and evaluation of interactive atmospheric chemistry in the Community Earth System Model. *Geoscientific Model Development*, *5*(2), 369–411. https://doi.org/10.5194/gmd-5-369-2012

Li, H., Cheng, J., Zhang, Q., Zheng, B., & He, K. (2019). Rapid transition in winter aerosol composition in Beijing from 2014 to 2017: Response to clean air actions. *Atmospheric Chemistry and Physics*. https://doi.org/10.5194/acp-2019-450

Li, M., Liu, H., Geng, G., Hong, C., Liu, F., Song, Y., et al. (2017). Anthropogenic emission inventories in China: A review. *National Science Review*, *4*(6), 834–866. https://doi.org/10.1093/nsr/nwx150

Liu, X., Zhu, B., Kang, H., Hou, X., Gao, J., Kuang, X., et al. (2021). Stable and transport indices applied to winter air pollution over the Yangtze River Delta, China. *Environmental Pollution*, *272*, 115954. https://doi.org/10.1016/j.envpol.2020.115954

Liu, Y., Warner, T. T., Bowers, J. F., Carson, L. P., Chen, F., Clough, C. A., et al. (2008). The Operational mesogamma-scale analysis and forecast system of the U.S. Army test and evaluation command. Part I: Overview of the modeling system, the forecast products, and how the products are used. *Journal of Applied Meteorology and Climatology*, *47*(4), 1077–1092. https://doi.org/10.1175/2007jamc1653.1

National Centers for Environmental Prediction/National Weather Service/NOAA/U.S. Department of Commerce. (2015). NCEP GDAS/FNL 0.25 degree global tropospheric analyses and forecast grids (updated daily). [Dataset]. *Research Data Archive at the National Center for Atmospheric Research, Computational and Information Systems Laboratory*. https://doi.org/10.5065/D65Q4T4Z-1686(93)90356-4

Pang, N., Gao, J., Che, F., Ma, T., Liu, S., Yang, Y., et al. (2020). Cause of $PM_{2.5}$ pollution during the 2016-2017 heating season in Beijing, Tianjin, and Langfang, China. *Journal of Environmental Sciences*, *95*(9), 9–209. https://doi.org/10.1016/j.jes.2020.03.024

Pathak, R. K., Wu, W. S., & Wang, T. (2009). Summertime $PM_{2.5}$ ionic species in four major cities of China: Nitrate formation in an ammonia-deficient atmosphere. *Atmospheric Chemistry and Physics*, *9*(5), 1711–1722. https://doi.org/10.5194/acp-9-1711-2009

Peng, W. (2024). Research data for manuscript entitled inconsistent 3-D structures and sources of sulfate ammonium and nitrate ammonium aerosols during cold front episodes. [Dataset]. https://doi.org/10.57760/sciencedb.15084

Petäjä, T., Järvi, L., Kerminen, V. M., Ding, A. J., Sun, J. N., Nie, W., et al. (2016). Enhanced air pollution via aerosol-boundary layer feedback in China. *Scientific Reports*, *6*(1), 18998. https://doi.org/10.1038/srep18998

Pleim, J. E., Bash, J. O., Walker, J. T., & Cooter, E. J. (2013). Development and evaluation of an ammonia bidirectional flux parameterization for air quality models. *Journal of Geophysical Research: Atmospheres*, *118*(9), 3794–3806. https://doi.org/10.1002/jgrd.50262

Pleim, J. E., Ran, L., Appel, W., Shephard, M. W., & Cady-Pereira, K. (2019). New bidirectional ammonia flux model in an air quality model coupled with an agricultural model. *Journal of Advances in Modeling Earth Systems*, *11*(9), 2934–2957. https://doi.org/10.1029/2019MS001728

Rodelas, R. R., Perdrix, E., Herbin, B., & Riffault, V. (2019). Characterization and variability of inorganic aerosols and their gaseous precursors at a suburban site in northern France over one year (2015-2016). *Atmospheric Environment*, *200*(MAR), 142–157. https://doi.org/10.1016/j.atmosenv.2018.11.041

Rolph, G., Stein, A., & Stunder, B. (2017). Real-time environmental applications and display sYstem: READY. *Environmental Modelling and Software*, *95*, 210–228. https://doi.org/10.1016/j.envsoft.2017.06.025

Saikawa, E., Kim, H., Zhong, M., Avramov, A., Zhao, Y., Janssens-Maenhout, G., et al. (2017). Comparison of emissions inventories of anthropogenic air pollutants and greenhouse gases in China. *Atmospheric Chemistry and Physics*, *17*(10), 6393–6421. https://doi.org/10.5194/acp-17-6393-2017

Seinfeld, J. H., & Pandis, S. N. (1998). *Environment: Science and Policy for Sustainable Development*, *40*, 7–26. https://doi.org/10.1080/00139157.1999.10544295

Shao, P., Tian, H., Sun, Y., Liu, H., Wu, B., Liu, S., et al. (2018). Characterizing remarkable changes of severe haze events and chemical compositions in multi-size airborne particles (PM_1, $PM_{2.5}$ and PM_{10}) from January 2013 to 2016–2017 winter in Beijing, China. *Atmospheric Environment*, *189*, 133–144. https://doi.org/10.1016/j.atmosenv.2018.06.038

Shi, S., Zhu, B., Lu, W., Yan, S., Fang, C., Liu, X., et al. (2021). Estimation of radiative forcing and heating rate based on vertical observation of black carbon in Nanjing, China. *The Science of the Total Environment*, *756*, 144135. https://doi.org/10.1016/j.scitotenv.2020.144135

Stein, A. F., Draxler, R. R., Rolph, G. D., Stunder, B. J. B., Cohen, M. D., & Ngan, F. (2015). NOAA's HYSPLIT atmospheric transport and dispersion modeling system. *Bulletin of the American Meteorological Society*, *96*(12), 2059–2077. https://doi.org/10.1175/bams-d-14-00110.1

Sun, P., Nie, W., Chi, X., Xie, Y., Huang, X., Xu, Z., et al. (2019). Two years of online measurement of fine particulate nitrate in the western Yangtze River Delta: Influences of thermodynamics and N_2O_5 hydrolysis. *Atmospheric Chemistry and Physics*, *18*(23), 17177–17190. https://doi.org/10.5194/acp-18-17177-2018

Sun, P., Nie, W., Wang, T., Chi, X., Huang, X., Xu, Z., et al. (2020). Impact of air transport and secondary formation on haze pollution in the Yangtze River Delta: In situ online observations in Shanghai and Nanjing. *Atmospheric Environment*, *225*, 117350. https://doi.org/10.1016/j.atmosenv.2020.117350

Tsinghua University. (2010). Multi-resolution emission inventory for China, version 1.3. Retrieved from http://meicmodel.org/

Vang, G., Wang, Y., Zeng, Y., Gao, G. F., Liang, X., Zhou, M., et al. (2013). Rapid health transition in China, 1990-2010: Findings from the Global Burden of Disease Study 2010. https://doi.org/10.1016/S0140-6736(13)61097-1

Wang, T., Huang, X., Wang, Z., Liu, Y., Zhou, D., Ding, K., et al. (2020). Secondary aerosol formation and its linkage with synoptic conditions during winter haze pollution over eastern China. *The Science of the Total Environment*, *730*, 138888. https://doi.org/10.1016/j.scitotenv.2020.138888

Wang, Y., Zhang, X. Y., & Draxler, R. R. (2009). TrajStat: GIS-based software that uses various trajectory statistical analysis methods to identify potential sources from long-term air pollution measurement data. *Environmental Modelling and Software*, *24*(8), 938–939. https://doi.org/10.1016/j.envsoft.2009.01.004

Wang, Y. S., Yao, L., Wang, L. L., Liu, Z. R., Ji, D. S., Tang, G. Q., et al. (2014). Mechanism for the formation of the January 2013 heavy haze pollution episode over central and eastern China. *Science China Earth Sciences*, *57*(1), 14–25. https://doi.org/10.1007/s11430-013-4773-4

Wei, Y., Li, J., Wang, Z.-F., Chen, H.-S., Wu, Q.-Z., Li, J.-J., et al. (2017). Trends of surface $PM_{2.5}$ over Beijing–Tianjin–Hebei in 2013–2015 and their causes: Emission controls vs. meteorological conditions. *Atmospheric and Oceanic Science Letters*, *10*(4), 276–283. https://doi.org/10.1080/16742834.2017.1315631

Xu, Q., Wang, S., Jiang, J., Bhattarai, N., Hao, J., Chang, X., et al. (2019). Nitrate dominates the chemical composition of $PM_{2.5}$ during haze event in Beijing, China. *The Science of the Total Environment*, *689*, 1293–1303. https://doi.org/10.1016/j.scitotenv.2019.06.294

Zhai, S., Jacob, D. J., Wang, X., Liu, Z., Liao, H., Shah, V., et al. (2021). Control of particulate nitrate air pollution in China. *Nature Geoscience*, *14*(6), 1–7. https://doi.org/10.1038/s41561-021-00726-z

Zhao, B., Wang, S., Wang, J., Fu, J. S., Liu, T., Xu, J., et al. (2013). Impact of national NOx and SO_2 control policies on particulate matter pollution in China. *Atmospheric Environment*, *77*, 453–463. https://doi.org/10.1016/j.atmosenv.2013.05.012

Zhao, X. J., Zhao, P. S., Xu, J., Meng, W., Pu, W. W., Dong, F., et al. (2013). Analysis of a winter regional haze event and its formation mechanism in the North China Plain. *Atmospheric Chemistry and Physics*, *13*(11), 5685–5696. https://doi.org/10.5194/acp-13-5685-2013

Zheng, G. J., Duan, F. K., Su, H., Ma, Y. L., Cheng, Y., Zheng, B., et al. (2015). Exploring the severe winter haze in Beijing: The impact of synoptic weather, regional transport and heterogeneous reactions. *Atmospheric Chemistry and Physics*, *15*(6), 2969–2983. https://doi.org/10.5194/acp-15-2969-2015